Journal of Biomolecular NMR (2006) 34: 245–257
DOI 10.1007/s10858-006-0026-6

Article

Band-selective ^{13}C homonuclear 3D spectroscopy for solid proteins at high field with rotor-synchronized soft pulses

Donghua H. Zhou, Kathryn D. Kloepper, Kem A. Winter & Chad M. Rienstra*
Department of Chemistry, Department of Biochemistry, and Center for Biophysics and Computational Biology, University of Illinois, 600 South Mathews Avenue, Urbana, IL 61801, USA

Received 21 November 2005; Accepted 20 February 2006

Key words: CCC 3D, CSA, dispersion, resolution, selective pulse, solid-state NMR

Abstract

We demonstrate improved 3D ^{13}C–^{13}C–^{13}C chemical shift correlation experiments for solid proteins, utilizing band-selective coherence transfer, scalar decoupling and homonuclear zero-quantum polarization transfer. Judicious use of selective pulses and a z-filter period suppress artifacts with a two-step phase cycle, allowing higher digital resolution in a fixed measurement time. The novel correlation of C^{ali}–C^{ali}–CX (C^{ali} for aliphatic carbons, CX for any carbon) reduces measurement time by an order of magnitude without sacrificing digital resolution. The experiment retains intensity from side-chain carbon resonances whose chemical shift dispersion is critical to minimize spectral degeneracy for large proteins with a predominance of secondary structure, such as β-sheet rich fibrillar proteins and α-helical membrane proteins. We demonstrate the experiment for the β1 immunoglobulin binding domain of protein G (GB1) and fibrils of the A30P mutant of α-synuclein, which is implicated in Parkinson's disease. Selective pulses of duration comparable the rotor period give optimal performance, but must be synchronized with the spinning in non-trivial ways to minimize chemical shift anisotropy recoupling effects. Soft pulses with a small bandwidth-duration product are best for exciting the ~70 ppm bandwidth required for aliphatic-only dimensions.

Introduction

Assignment and structure determination for uniformly ^{13}C- and ^{15}N-labeled proteins by solid-state NMR (SSNMR) have so far relied strongly upon 2D ^{13}C–^{13}C homonuclear and 2D or 3D NC′CX and NC$^{\alpha}$CX heteronuclear correlation experiments, which are necessary for the identification of amino acid type and establishing sequential connectivity (Sun et al., 1997; Hong, 1999; Rienstra et al., 2000; Pauli et al., 2001; Franks et al., 2005). However, C^{α} and C′ chemical shifts are known to vary within amino acid residue types based primarily on secondary structure (Wishart et al., 1991). Therefore, helix-rich proteins usually have limited backbone chemical shift dispersion (Powers et al., 1992). Likewise, highly β-sheet rich proteins such as fibrillar aggregates tend to have modest chemical shift dispersion (Antzutkin et al., 2002; Balbach et al., 2002; Petkova et al., 2002). Spectral overlap is also expected for large proteins (> 50 kDa). Therefore, additional correlation schemes are desired to lift spectral degeneracy in such proteins.

Homonuclear ^{13}C–^{13}C–^{13}C 3D correlation makes optimal use of the chemical shift dispersion available from each backbone and side chain ^{13}C resonance. However, sampling the large bandwidth (~200 ppm) required for all carbons results in very long acquisition times. For example, an experiment digitized in each indirect dimension to 1 ppm, with a 2 s recycle delay and 2-step phase cycle would require 7.5 days. Such long

*To whom correspondence should be addressed. E-mail: rienstra@scs.uiuc.edu

acquisition time is wasteful of instrument time in the sampling-limited cases (Szyperski et al., 2002), and even in sensitivity-limited cases it may be preferable to break the whole experiment into multiple short runs due to interruptions caused by service outages and cryogen fills. Double quantum evolution used in a previous study requires a long phase cycle (16 steps) and hence further lengthens acquisition time, though each peak is encoded with at least two frequencies (Heise et al., 2005b).

In solution NMR, such problems have traditionally been solved by judicious choice of indirect dimension aliasing (Kay et al., 1989; Bax et al., 1991), so that, for example, carbonyl resonances would appear near the aliphatic region. Unfortunately in magic-angle spinning experiments, such folding strategies are often complicated by manifolds of side bands that in general will arise in inconvenient locations; to avoid these side bands altogether requires relatively high spinning rates that exclude the use of large volume rotors. Furthermore, aromatic resonances in solid proteins present an additional complication in ^{13}C-detected SSNMR experiments that is not typically encountered in amide ^{1}H-detected solution NMR.

Another approach often used in solution NMR is to extend the digital resolution of processed data sets with linear prediction (Barkhuijsen et al., 1987). This strategy works well when time-domain trajectories have high signal-to-noise ratio and consist of a small number of frequency components that are well-described by simple exponentially damped cosine functions. Unfortunately in SSNMR, the ^{13}C line shapes in particular are likely to be complicated both by scalar and residual dipolar contributions, and the sensitivity is relatively low. These facts have impaired the application of forward linear prediction methods to SSNMR 3D data.

Therefore improved methods for addressing this spectroscopic problem are required. Here we demonstrate that the use of band-selective coherence filters greatly improves the achievable digital resolution for 3D homonuclear SSNMR experiments. Specifically, C^{ali}–C^{ali}–CX correlation, where C^{ali} refers to all aliphatic and CX to all ^{13}C resonances, saves digitization time by a factor of $\sim$9 by reducing the required bandwidth. Moreover, we show that two-step phase cycles are sufficient to suppress all significant artifacts, even without gradients, which are not yet commonly available on SSNMR probes. We show that this experiment preserves the chemical shift dispersion inherent to broadband pulse sequences, but at a greatly reduced experiment time: complete 3D data sets are acquired within 14 h on a 750 MHz instrument with 1 ppm digital resolution in the indirect dimensions and 1.5 s recyle delay.

In order to achieve these gains, we have found it necessary to restrict phase cycles to two steps. Narrower band selectivity for C^{α}—CO—CX was previously demonstrated (Straus et al., 1996), by employing a pair of soft (Gaussian) and hard π pulses in the middle of indirect evolution periods. This sequence achieved both band selectivity and homonuclear J-decoupling, and could be used for C^{ali}–C^{ali}–CX correlation in the limit of larger bandwidth pulses; however, as originally published a minimum of four steps were required in the phase cycle, and we have not yet found a satisfactory solution for a two-step phase cycle in this sequence, because the soft π pulses in the two indirect dimensions need to be phase cycled independently. Instead, we achieve excellent artifact suppression with a two-step phase cycle in our implementation by using a soft $\pi/2$ pulse followed by a z-filter to selectively destroy CO for the t_1 dimension and the soft-hard π pair for the t_2 dimension.

The second issue that arises in the context of band-selective ^{13}C experiments is the interference between soft pulses and magic-angle spinning (MAS). Selective pulses under MAS have been employed for homonuclear decoupling (Straus et al., 1996), spin-state selection (Duma et al., 2003a; Duma et al., 2003b), and selective REDOR (Jaroniec et al., 2001a, 2001b). Most of these applications were performed at $\sim$500 MHz and so the effects of CSA were small, although two recent reports recognized relative phase differences of spinning center band and side bands due to selective pulses (Igumenova and McDermott, 2003; Veshtort and Griffin, 2004). In applications at higher B_0 field, the effects of chemical shift anisotropy (CSA) must be accounted for more explicitly. Recently it was found that for the soft-hard π pair, the soft pulse width needs to be of duration $(n + 1/2) * \tau_R$, where n is an integer and τ_R the rotor period, in order to preserve the intensity of the center band; in the limit where n is approximately 10, many soft pulses shift rotational echoes by $\tau_R/2$ (Li et al., 2006). This is typical of narrow-band selective soft pulses. However, in the

current study more complicated dependence is reported for pulses of duration comparable to the rotor period, which is necessary to excite the ~70 ppm aliphatic chemical shift region at high magnetic fields. This aspect of soft pulses under MAS is still not fully understood, and we leave the theoretical treatment and design of new soft pulses that compensate for the MAS dependence as future work. Here we focus on the empirical characterization of soft pulses, originally developed for solution NMR, in order to choose the best conditions for the band selective C^{ali}–C^{ali}–CX 3D magic-angle spinning experiments.

Materials and methods

Uniformly ^{13}C,^{15}N-labeled protein GB1 was prepared and packed into a 3.2 mm thin wall rotor according to Franks et al. (2005); in the central 80% length of this 36 μl rotor, ~22 mg of total material was packed, which was approximately two-thirds protein by mass, for a total of 15 mg (2.5 μmol) of GB1.

The A30P mutant of α-synuclein cDNA construct was expressed in *E.coli* BL21(DE3) competent cells and grown in Luria broth at 37 °C. At $OD_{600} = 0.70$, the cells were pelleted and resuspended into 1 l M9 minimal media containing 2 g ^{13}C-glucose, 1 g ^{15}N NH_4Cl, and ^{13}C, ^{15}N-Bioexpress (Cambridge Isotopes) at 10% of the recommended dose (Holdeman and Gardner, 2001). At $OD_{600} = 0.7$, protein expression was induced by the addition of IPTG. After 3 h, purification was performed by thermal lysis in the presence of strong base and protease inhibitors, followed by precipitation with $(NH_4)_2SO_4$, and hydrophobic interaction and gel exclusion chromatography, as described in detail elsewhere (Kloepper et al., 2006, in press). Sample purity was confirmed by gel electrophoresis and mass spectrometry. Solutions containing 1 mM αS, 0.10 mM EDTA, 0.02% NaN_3, 1% fibril seeds, and 50 mM phosphate buffer (pH 7.4) were incubated with agitation (250 rpm) at 37 °C. Fibrils were separated from solution by ultracentrifugation and packed directly into a 3.2 mm thin wall rotor; the gelatinous sample contained around 5 mg protein and large amount of water.

All experiments in this study were carried out on a 750 MHz Varian Inova spectrometer (188.5 MHz ^{13}C frequency) with VNMR 6.1C software (Varian NMR, Palo Alto, California). Each of the three channels was equipped with a waveform generator (WFG) capable of dividing radio frequency (RF) amplitude into 1024 steps. During the soft pulses, the RF amplitude was appropriately attenuated before feeding to the WFG for fine adjustments of the pulse shape. An actively biased transmit-receiver switch (Warner Harrison, Medfield, MA) was employed to provide optimal linearity in the transmitter response at low power; this circuit consists of a PIN diode circuit biased by a DC voltage, cascaded semi-rigid quarter wavelength cables, and an integrated GaAsFET preamplifier. The insertion loss was within measurement error the same for pulses ranging from 100 mV to ~100 V peak amplitude; for the high power pulses the forward power was measured with −50 dB attenuation through a directional coupler resulting in ~200 mV peak measured voltages. The correlation between forward power and γ B_1 nutation frequency on the ^{13}C channel of the probe was approximately 1 V per 1 kHz. The shaped pulses were created using Pbox library within the VNMR software. A Balun™ (Varian NMR) ^{1}H–^{13}C–^{15}N triple resonance 3.2 mm probe was configured in ^{1}H–^{13}C double resonance mode, which we observed to have ~30% higher ^{13}C sensitivity than in ^{1}H–^{13}C–^{15}N triple resonance mode. Sample spinning rates were typically 12.5 kHz. TPPM decoupling was employed with a moderate power of 70 kHz (Bennett et al., 1995). Hard π pulses were 2.5 μs for both ^{1}H and ^{13}C. For the ^{13}C–^{13}C 2D, the indirect dimension had 50 kHz spectral width and was digitized to 10 ms. For the 3D experiments, tangent ramped Hartman-Hahn cross polarization condition (70 kHz on ^{1}H, 70 kHz on ^{13}C, with ±7 kHz ramp on ^{13}C, carrier at 175 ppm) was chosen to maximize aliphatic signals (Hediger et al., 1994). The spectral width of 12.5 kHz was used for C^{ali} dimensions. The indirect dimensions were digitized to at least 5 ms (i.e., 1.06 ppm), principally limited by RF heating effects in this probe; higher digital resolution could be achieved with probes incorporating scroll resonators (Stringer et al., 2005). Each spectral dimension was zero filled to 20 ms prior to further processing with NMRPipe software (Delaglio et al., 1995).

The C^{ali}–C^{ali}–CX pulse sequence is shown in Figure 1 along with the 2-step phase cycle. The soft-hard π pair is used for in-band selection of

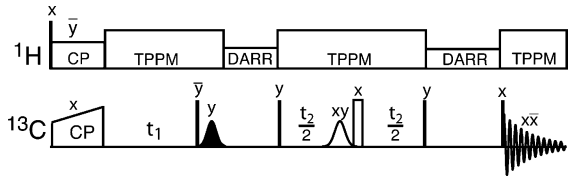

Figure 1. Band selective 3D C^{ali}–C^{ali}–CX pulse sequences used in this study. Filled and open narrow bars represent hard $\pi/2$ and π pulses, respectively; filled and open shaped pulses represent soft $\pi/2$ and π pulses, respectively. Carrier frequency is placed at 175 ppm, and jumps to 45 ppm during the soft π pulse using phase modulation. Two-step phases are noted beside the pulses. Quadrature detection of the indirect dimensions is achieved by varying phases of the receiver and the post-evolution hard $\pi/2$ pulses according to the TPPI-States protocol (Marion et al., 1989). TPPM proton decoupling (Bennett et al., 1995) and DARR homonuclear mixing (Takegoshi et al., 2001) are employed. The same pulse sequence can be used for C^{ali}–C′–CX experiment by omitting the frequency jump.

the aliphatic region in the t_2 dimension; the unwanted C′ magnetization is canceled by alternating the phase of the soft π pulse between x and y in successive scans (Straus et al., 1996). If the soft-hard π pair is also applied to the t_1 dimension for C^{ali} selection, the soft π pulses need to be independently phase cycled to avoid the unwanted C′–C^{ali}–CX pathway, resulting in a minimum of 4-step phase cycle for the whole sequence (Straus et al., 1996). Our sequence in Figure 1 achieves 2-step overall phase cycle by completely destroying undesired C′ magnetization before the t_2 evolution period. The hard $\pi/2$ pulse restores coherence back to the longitudinal direction, followed by a soft $\pi/2$ pulse to selectively excite the C′ region, which is then dephased during the z-filter. The dephasing of transverse C′ requires 10 ms for a normal z-filter where no ^{1}H power is applied, but only 1 ms if the ^{1}H channel is irradiated with $\nu_1 = \nu_R$ rotary-resonance condition to recouple ^{1}H–^{13}C dipolar interaction (Oas et al., 1989), where ν_1 is RF strength and ν_R is sample spinning frequency. This z-filter is therefore seamlessly integrated into the dipolar assisted rotational resonance (DARR) mixing period that requires the same irradiation power on ^{1}H channel (Takegoshi et al., 2001).

The carrier frequency is placed in the C′ region and jumps to the middle of aliphatic region during the soft π pulse in t_2 evolution by phase modulation (in steps of 15° or less). Without the frequency jump, the sequence correlates C^{ali}–C′–CX.

Results

Performance of soft π and π/2 pulses under MAS

The performance of the soft-hard π pair is characterized for in-band selection in Figure 2. It has been recently reported for rSNOB (Kupce et al., 1995) pulses of duration ~1 ms, efficient refocusing of the soft-hard π pair required the duration of the soft pulse to be $(n+0.5) * \tau_R$, where n is integer and τ_R the rotor period; numerical simulations showed that the soft π pulse caused the rotational echo to shift by half a rotor period (Li et al., 2006). Consistent with this previous result, in Figure 2(a) for rSNOB, at long pulse widths (>560 μs) the refocusing efficiency of the C′ center band is nearly constant for the soft pulse alone and exhibits minima at $n^*\tau_R$ and maxima at $(n+0.5)^*\tau_R$ for soft-hard pair. However, for shorter pulses, the efficiency for the soft pulse alone starts to oscillate with period of $2^*\tau_R$, having maxima at $2n^*\tau_R$ and minima at $(2n+1)^*\tau_R$. The efficiency for the soft-hard pair exhibits shallower valleys at $2n^*\tau_R$ and deeper valleys around $(2n+1)^*\tau_R$; meanwhile pulse width values for the best efficiency shift toward $2n^*\tau_R$. For a simple Gaussian pulse (Bauer et al., 1984) the same phenomenon is observed except for a shorter threshold pulse width (~ 400 μs, data not shown). For REBURP (Geen and Freeman, 1991) in Figure 2(b), the transition takes place at a much longer pulse width (> 1.5 ms).

The threshold pulse width appears to correlate with the bandwidth-duration product (WT) and attenuation factor Δ, the power needed relative to a rectangular π pulse of the same width: WT = 0.9 and Δ = −7.7 dB for Gaussian π pulse truncated at 1%, WT = 1.85 and Δ = −13.5 dB for rSNOB, and WT = 4.88 and Δ = −21.9 dB for REBURP, with the WT values taken directly from the Pbox library and Δ values calculated from the pattern files generated by Pbox. As the B_1 field increases, HORROR (Nielsen et al., 1994) and/or rotary resonance recoupling (Oas et al., 1989) conditions may be encountered. For example, with a 320 μs pulse width, the maximum B_1 fields were 3.8, 7.4, and 19.4 kHz for the Gaussian, rSNOB, and REBURP shapes, respectively. Therefore, the simplest approach to minimize interference effects is to use Gaussian pulses, but this solution still does not avoid the resonance conditions and gives a

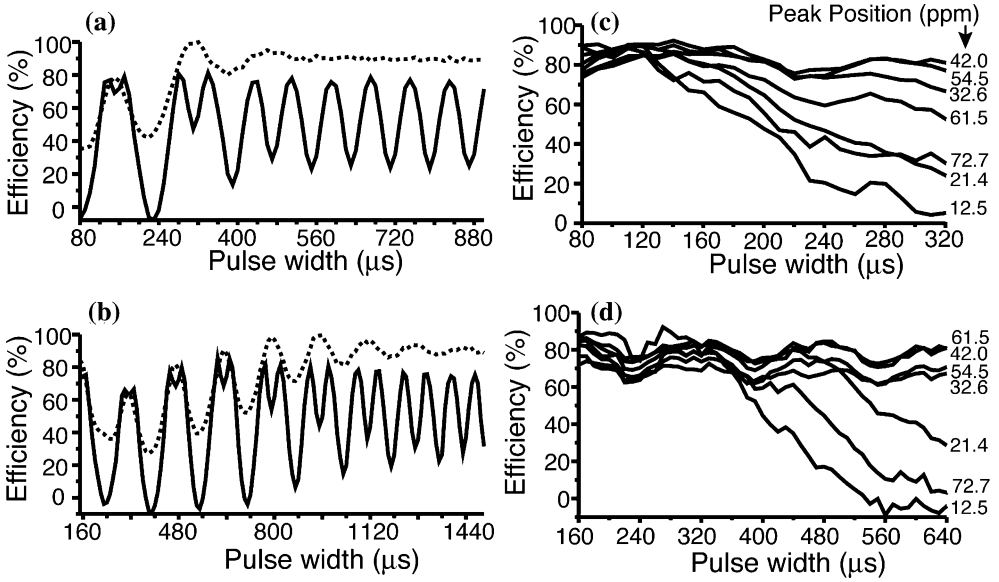

Figure 2. Characterization of selective π pulses with the protein GB1 at 12.5 kHz MAS rate (80 μs rotor period). (a) C′ center band refocusing efficiency of rSNOB soft π (dotted line) and soft π-hard π pair (solid line); the on-resonance efficiency (at 175 ppm) is plotted. (b) Repeat (a) for REBURP soft pulse. (c) Refocusing efficiencies in aliphatic region for rSNOB soft π-hard π pair, with carrier positioned at 45 ppm. (d) Repeat (c) for REBURP. The ~ 10 μs offset from integer rotor periods of the local minima in (a) and (b) includes ~ 6μs hardware delay in the WFG and power level resetting and part of the finite pulse width for the hard π pulse (5 μs).

significant excitation far from resonance, unlike the more ideal rSNOB and REBURP profiles. Refocusing efficiencies for peaks spanning the whole aliphatic region are shown for rSNOB and REBURP in Figure 2(c) and Figure 2(d), respectively. The $2^*\tau_R$ periodicity is also visible but much weaker than in the C′ region, due to the smaller aliphatic CSA. For the 3D experiments, 120 μs rSNOB was chosen for uniform refocusing efficiency of 87 ± 3% for the whole aliphatic region.

The relation of excitation efficiency of soft π/2 pulses to pulse width is shown in Figure 3. The efficiency is close to constant for relatively long pulses for 3π/2 sinc (one lobe on each side, WT = 1.42) (Hutchinson et al., 1978), eSNOB (WT = 1.42) (Kupce et al., 1995), 3π/2 Gaussian (1% truncation, WT = 1.4) (Emsley and Bodenhausen, 1989), and EBURP2 (WT = 4.6) (Geen and Freeman, 1991). For the former three, the efficiency experiences a minimum when the pulse width is τ_R and $2^*\tau_R$ for EBURP2. Gaussian cascades G^4 (WT = 7.47) (Emsley and Bodenhausen, 1990) and broad band excitation pulses made of cosine series (having large WT ≥9, efficiency plot not shown) (Abramovich and Vega, 1993) have more complicated dependence and inferior efficiency in the range investigated (below 1.2 ms).

For the C′ excitation by soft π/2 pulses, we found that the 3π/2 sinc and eSNOB pulses achieved close to 100% efficiency at their optimal pulse widths. The 3π/2 sinc has a pure phase excitation profile due to a favorable trajectory similar to that for the 3π/2 gaussian (Emsley and Bodenhausen, 1989). From 220 to 370 μs, the excitation efficiency of the 3π/2 sinc has near constant efficiency and 320 μs could be used for 24 ppm bandwidth.

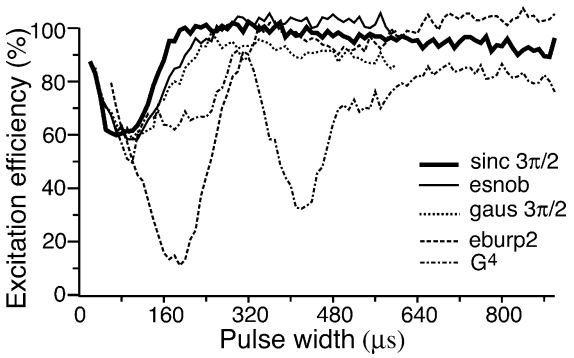

Figure 3. Soft π/2 pulse performance at 12.5 kHz MAS rate (80 μs rotor period). The excitation efficiency of an on-resonance C′ peak at 175 ppm is shown.

The selectively excited C′ signal was then dephased by the z-filter, retaining close to 90% of the aliphatic signal intensity. Similar efficiency can be achieved by $\pi/2$ sinc, which is also able to completely remove C′ this way; its phase distortion in C′ excitation does not present a problem here since C′ signal is destroyed.

C^{ali}–C^{ali}–CX 3D experiments

Figure 4(a) is a ^{13}C–^{13}C 2D spectrum acquired with 20 ms DARR mixing. Figure 4(b) shows the $F_2 = 54.6$ ppm plane of a C^{ali}–C^{ali}–CX, which is completed in 14 h with 1 ppm digitization in the indirect dimensions. Compared to the 2D spectrum, the plane of the 3D has only a small fraction of peaks. Therefore it is much easier to identify peaks belonging to a same residue; peak assignments are performed as consistent with previous work (Table 1 in Franks et al., 2005). This plane resolves several alanines in the C^{β} diagonal and C^{α}–C^{β} cross peaks, methionine α through γ, lysine α and β (K4 peaks appear weak only because they are not centered on this plane). The resolution in the C′ region is very good due to the large C′ dispersion for these residues.

With nearly all carbons included in each dimension, the chance of degeneracy is greatly reduced. For instance, out of the 10 threonines in the GB1 sequence, 3, 4, and 1 of them appear in the C^{α}, C^{β}, and C^{γ} planes of Thr18, respectively (Figure 5). For residues with short side chains, such as several Thr, Val and Ala residues, nearly the whole spin systems appear in a single plane, with intensities varying according to the coherence pathway. Among the T18 peaks, T18C^{α}—C^{γ}—C′ is the weakest, since it has the longest polarization transfer pathway. T18C^{β}—C^{γ}—C^{α} and T18C^{γ}—C^{γ}—C^{α} peaks are stronger due to their shorter transfer pathways.

The lysine spin system is in general difficult to identify completely in CC 2D spectra because of degeneracy with leucines and other lysines. However, the task is simplified by the C^{ali}–C^{ali}–CX 3D spectrum since all carbon sites provide some dispersion. Spin systems of all six lysines in GB1 can be identified and the K13 network is illustrated in Figure 6. Empirically the DARR mixing facilitates magnetization transfer in 5–6 ms per step through the covalently bonded nuclei. The second mixing time of 20 ms allowing 3- to 4-bond

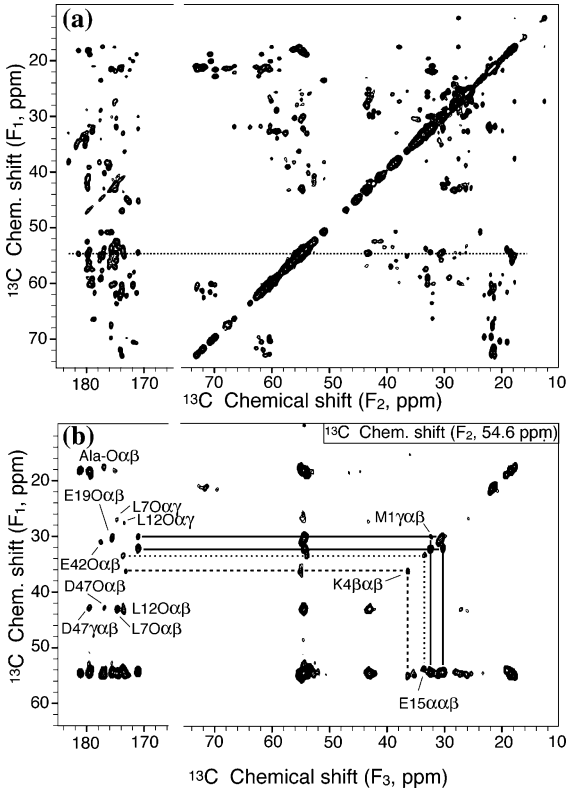

Figure 4. ^{13}C–^{13}C 2D and C^{ali}–C^{ali}–CX 3D spectra of GB1 at 750 MHz. (a) ^{13}C–^{13}C 2D acquired in 1 h with 10 ms evolution time and 50 kHz spectral width in the indirect dimension, 15 ms evolution in the direct dimension, and 20 ms DARR mixing. A dotted line is drawn at $F_1 = 54.6$ ppm. (b) The $F_2 = 54.6$ ppm plane of a C^{ali}–C^{ali}–CX 3D spectrum acquired in 14 h with 5 ms evolution time and 12.5 kHz spectral width in each indirect dimension and 10 and 20 ms DARR for the first and second mixing periods, respectively. Sample spinning speed was 12.5 kHz, recycle delay was 1.5 s, and temperature was regulated at 0°C. Each dimension of all spectra was zero filled to 20 ms resolution and apodized with 25 and 50 Hz line broadening for 2D and 3D, respectively. Contours separated by a factor of 1.2 starting from 15 and 6 times the root mean square (r.m.s) noise level for 2D and 3D, respectively.

transfer was chosen for long side chain residues like lysine, leucine, etc; longer mixing time may result in less intense 1- and 2-bond correlations.

However, if inter-residue correlations are sought, mixing times of 100 ms or longer can be used, as previously demonstrated in ^{13}C–^{13}C 2D experiments (Castellani et al., 2002; Zech et al., 2005). The interpretation is greatly simplified with the 3D spectra. For example, Figure 7 is the C^{ali}–C^{ali}–CX 3D spectrum of GB1 acquired with 100 ms DARR mixing for the second polarization transfer. The F_1 plane centered at A20 C^{α} chemical

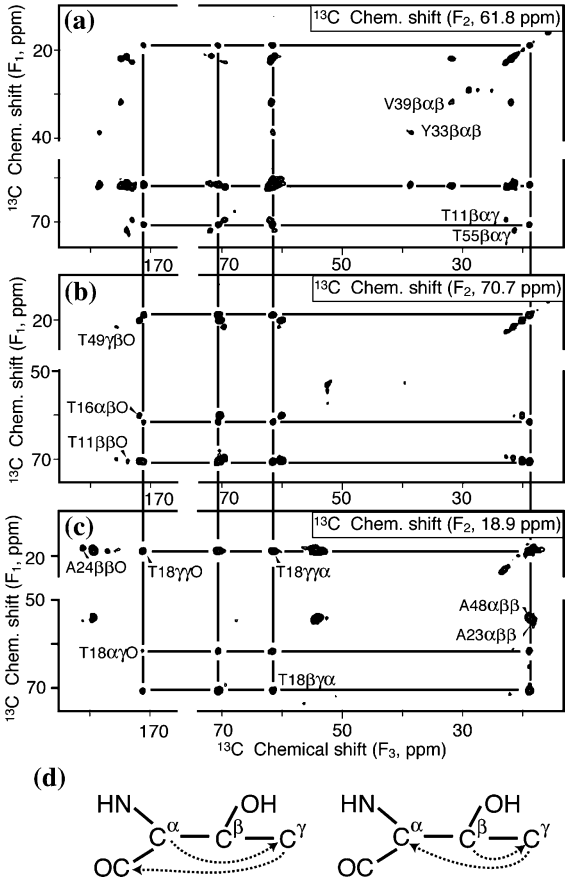

Figure 5. Representative short side chain residues in C^{ali}–C^{ali}–CX 3D spectrum of protein GB1. The spin system of residue T18 is traced by a network of lines. (a) C^{α} plane at $F_2 = 61.8$ ppm. (b) C^{β} plane at $F_2 = 70.7$ ppm. (c) C^{γ} plane at $F_2 = 18.9$ ppm. (d) The transfer pathways for two peaks C^{α}—C^{γ}–C' and C^{β}—C^{γ}—C^{α}. See Figure 4 for data acquisition and processing details.

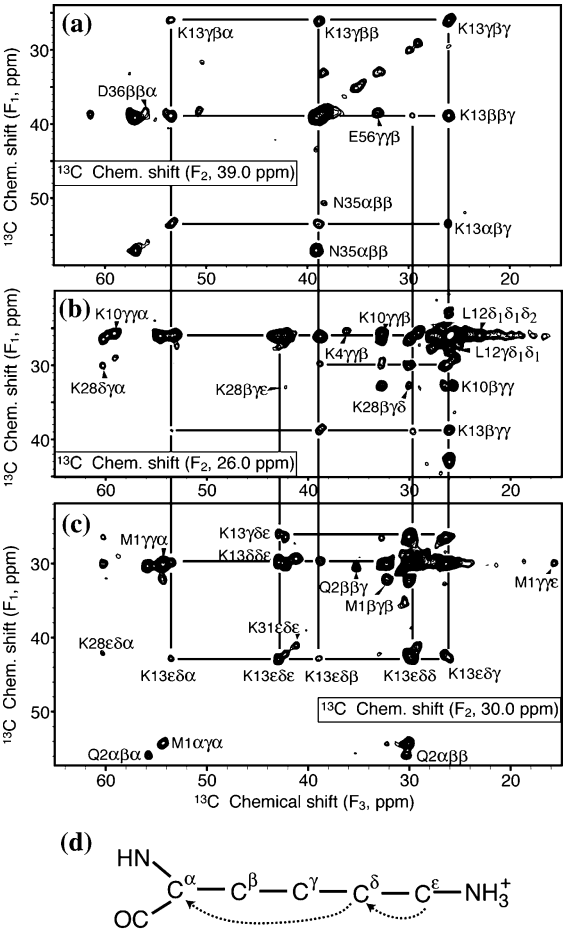

Figure 6. Representative long side chain residues in C^{ali}–C^{ali}–CX 3D spectra of protein GB1. The spin system of residue K13 is traced by a network of lines. (a) C^{β} plane at $F_2 = 39$ ppm. (b) C^{γ} plane at $F_2 = 26$ ppm. (c) C^{δ} plane at $F_2 = 30$ ppm. (d) The transfer pathway for peak C^{ε}—C^{δ}—C^{α}. See Figure 4 for data acquisition and processing details.

shift (Figure 7(a)) shows inter-residue C^{α}—C^{α} cross peak between A20 and E19. The G38 plane in Figure 7(b) shows cross peaks from G38 C^{α} to N37 C^{α}, V39 C^{α} and $C^{\gamma 1}$, and D40 C^{α} and C^{β}.

Application of the C^{ali}–C^{ali}–CX 3D experiment to α-synuclein fibrils is shown together with a ^{13}C–^{13}C 2D spectrum for comparison in Figure 8. For this gelatinous sample containing a large amount of water, the experiment was carried out at low temperature (−50 °C) so that the side-chain dynamics were minimized, to enable efficient hetero- and homonuclear polarization transfer. This is an example of a sensitivity-limited experiment: the whole 74-h acquisition was broken in two identical runs, which were co-added. The A30P synuclein sequence is abundant in several amino acids: 10 Thr, 15 Lys, 18 Glu, 18 Gly, 18 Ala, and 19 Val. Many of these amino acids are in similar chemical environments within seven imperfect 11-mer repeats (Clayton and George, 1998). These properties result in a 2D ^{13}C–^{13}C spectrum with substantial overlap among these residues. With improved resolution in the C^{ali}–C^{ali}–CX 3D, amino acid types can be easily identified: threonines in Figure 8(i), valines in (h) and (c), glutamines and a helical alanine in (g), β-turn alanines in (f), β-sheet alanines in (e), and lysines/leucines in (d). In combination with established 3D methods (Sun et al., 1997; Hong, 1999; Rienstra et al., 2000; Pauli et al., 2001;

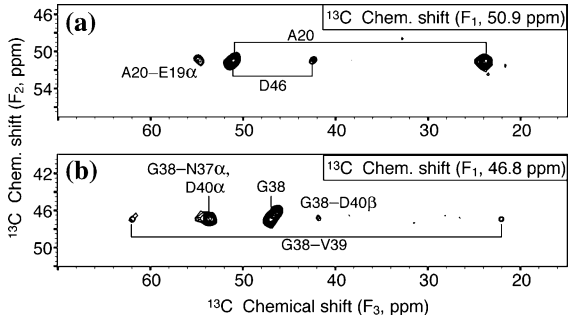

Figure 7. C^{ali}–C^{ali}–CX 3D spectra of GB1 with long mixing time. (a) $F_1 = 50.9$ ppm plane (b) $F_1 = 46.8$ ppm plane of a C^{ali}–C^{ali}–CX 3D spectrum acquired in 23 h with 8 ms evolution time for the second dimension and 100 ms for the second DARR mixing, processed with 100 Hz line broadening (−40 Hz exponential, 140 Hz Gaussian). All other parameters are the same as in Figure 4(b). Contours were separated by a factor of 1.15 starting from 5 times the r.m.s noise level.

Franks et al., 2005), the 3D CCC experiment can be utilized to perform unambiguous sequential assignments. The efficient assignment of samples such as A30P synuclein will be critical in order to understand the polymorphisms in fibril samples that can arise from differences in sample environment or protein sequence (Heise et al., 2005a).

Discussion

The NCC 3D experiment (Sun et al., 1997; Hong, 1999; Rienstra et al., 2000; Pauli et al., 2001; Franks et al., 2005) uses ramped SPECIFIC CP (Baldus et al., 1998) to transfer magnetization from N_i to either C_i^{α} for intra-residue correlation or to $C'_i{-}1$ for inter-residue connection. Magnetization is then propagated to other carbon sites by homonuclear recoupling within residue *i* for NCACX or *i-1* for NC′CX. It is not uncommon to find two or more residues with degenerate ^{15}N and $^{13}C^{\alpha}$ chemical shifts, and these residues fail to be resolved in NCACX. Similar difficulty can also be encountered for NC′CX. Some of the side chain ^{13}C sites still have a significant likelihood of non-degenerate chemical shifts. Such chemical dispersion can be fully utilized in a ^{13}C–^{13}C–^{13}C 3D spectrum to identify the whole ^{13}C spin system for a residue. The obtained chemical shifts can be used to assist the sequential assignment process in combination with ^{15}N-based methods.

The NCC experiments usually have weak or no intensity for ^{13}C sites at the end of long side chains, for two reasons: (1) usually only ~50% magnetization can be transferred from N to C^{α} or C′; (2) short mixing times for the homonuclear

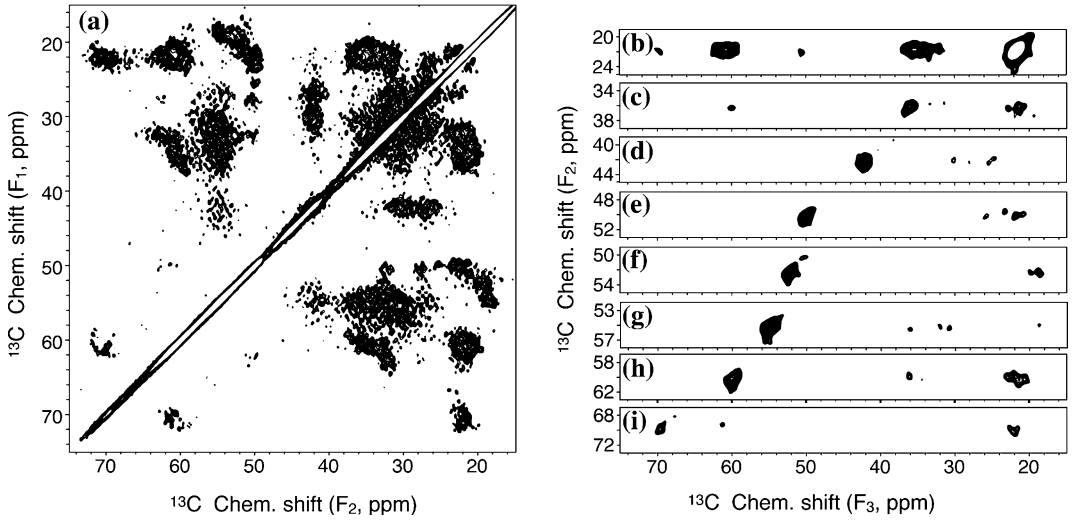

Figure 8. Spectra of A30P mutant α-synuclein fibrils at −50 °C. (a) ^{13}C–^{13}C 2D spectrum acquired in 30 h with 25 ms DARR mixing, 10 ms evolution time in the indirect dimension, and processed with 25 and 40 Hz net line broadening direct and indirect dimensions, respectively. Contours were drawn starting from 6 r.m.s noise lelvel, and separated by a factor of 1.1. (b)–(i) $F_1 = 21.7$, 36.3, 42.3, 50.2, 52.5, 55.3, 60.2, 69.8 ppm planes of a C^{ali}–C^{ali}–CX 3D spectrum acquired in two 37-h runs, all parameters are the same as in Figure 4(b) except for a longer recycle delay of 2 s. The 3D was processed with 100 Hz net line broadening in each dimension (−40 Hz exponential, 140 Hz Gaussian). Contours were drawn starting from 5 times the r.m.s noise level, and separated by a factor of 1.05.

transfer (e.g. <20 ms DARR) are preferred for most residues; longer mixing time may result in polarization accumulation at the terminal site(s) of side chain and leave very weak C^{α} and C^{β} (e.g. for valines). The mixing times optimized for short chain residues are not long enough to populate the far end of long chain residues. Even when a long mixing time is used, the intensity could become too weak for each site since the magnetization is distributed too sparsely. In a C^{ali}–C^{ali}–CX 3D experiment, however, all ^{13}C sites (except C′) have their own initial polarization instead of relying on polarization arising from the backbone sites. Moderate mixing times (~20 ms for transfer up to 4 bonds) work well for residues of short side-chains, allowing the reconstruction of spin systems of long side-chains by assembling several planes (c.f. Figure 6).

In most of our experiments, relatively short DARR mixing times (≤ 20 ms) have been used to maximize the intensity of two- and three-bond intraresidue correlations. However, if the interresidue contact information is desired, long mixing times (>100 ms) can be utilized. With additional resolution in the 3D experiment, these interresidue peaks are relatively easy to identify, as in Figure 7, and provide valuable correlations for establishing sequential assignments. Other methods such as RFDR, proton driven spin diffusion, and proton mediated spin diffusion, can also be applied for the second homonuclear mixing (Bloembergen, 1949; Suter and Ernst, 1982, 1985; Kubo and McDowell, 1988; Bennett and Griffin, 1992; Heise et al., 2005b).

Among the existing soft pulses developed for solution NMR study, those having small bandwidth-duration product are best suited for application in MAS SSNMR. The efficiency of the C^{ali} selection is around 85% using currently available soft pulses, for both the soft-hard π pair and the soft π/2 plus z-filter approaches. The two selection steps in the 3D experiment result in ~30% intensity loss. Before more efficient broadband selective components can be designed, we need to better understand the complicated dependence on pulse width observed in this study on the basis of the interplay among the soft pulse, CSA and sample spinning. Theoretical treatments so far have only been attempted for long pulse widths of integer rotor periods (Igumenova and McDermott, 2003; Veshtort and Griffin, 2004); these studies reveal that both amplitude and phase of the soft pulse are virtually modified by the CSA, rendering additional orientation dependence. Numerical simulations have been used to show a half rotor period shift by a soft π pulse in the long pulse limit (Li et al., 2006). Theoretical treatment of short pulses of non-integer rotor period duration will be investigated separately to explain the phenomenon observed here. Insights gained will enable improved soft pulses to be specifically designed for MAS SSNMR.

Nevertheless, in its optimal implementation so far, the soft-hard π pair has ~85% refocusing efficiency. The initial signal loss in the first row of the indirect dimension is justified when one considers the slower decay in the J-decoupled interferogram. The integrated intensities (reduced by transverse relaxation time T_2) are

$$I_1 = \frac{1}{T_2}\int_0^{t_{\max}} \xi e^{-t/T_2} dt = \xi(1 - e^{-t_{\max}/T_2}) \qquad (1)$$

for J-decoupled experiments, where ξ is the refocusing efficiency and $t_{\max}$ the evolution time, and

$$\begin{aligned} I_2 &= \frac{1}{T_2}\int_0^{t_{\max}} e^{-t/T_2} |\cos(\pi J t)| dt \\ &= g(t_{\max}) - g(0) \\ &= \frac{1}{1+(\pi J T_2)^2}\{1 + e^{-t_{\max}/T_2} \\ &\quad \times [-\cos(\pi J t_{\max}) + \pi J T_2 \sin(\pi J t_{\max})]\} \end{aligned} \qquad (2a)$$

for non-decoupled experiments when $t_{\max} \leq 1/2J$, where

$$g(t) = \frac{e^{-t/T_2}}{1+(\pi J T_2)^2}[-\cos(\pi J t) + \pi J T_2 \sin(\pi J t)] \qquad (2b)$$

and

$$\begin{aligned} I_2 &= -g(t_{\max}) + 2g\left(\frac{1}{2J}\right) - g(0) \\ &= \frac{1 + 2\pi J T_2 e^{-1/2JT_2}}{1+(\pi J T_2)^2} + \frac{e^{-t_{\max}/T_2}}{1+(\pi J T_2)^2} \\ &\quad \times [\cos(\pi J t_{\max}) - \pi J T_2 \sin(\pi J t_{\max})] \end{aligned} \qquad (2c)$$

when $1/2J \leq t_{\max} \leq 3/2J$. Equations (1) and (2) apply to glycine which has only C′ and C^{α} coupling $J_{O\alpha}$. For other amino acids, we also need to consider $J_{\alpha\beta}$, the coupling between C^{α} and C^{β}. In this case, when $J_{O\alpha}$ is decoupled, the intensity is

$$I'_1 = \frac{1}{T_2}\int_0^{t_{\max}} \xi e^{-t/T_2}|\cos(\pi J_{\alpha\beta}t)|dt = \xi I_2|_{J=J_{\alpha\beta}} \tag{3}$$

The non-decoupled intensity is

$$\begin{aligned} I'_2 &= \frac{1}{T_2}\int_0^{t_{\max}} e^{-t/T_2}|\cos(\pi J_{O\alpha}t)\cos(\pi J_{\alpha\beta}t)|dt \\ &= \frac{1}{2T_2}\int_0^{t_{\max}} e^{-t/T_2}|\cos(\pi J_{O\alpha}t) + \cos(\pi J_{\alpha\beta}t)|dt \\ &= \frac{1}{2}\left\{[g(t_{\max}) - g(0)]\Big|_{J=J_{O\alpha}+J_{\alpha\beta}} \right. \\ &\qquad \left. + [g(t_{\max}) - g(0)]|_{J=J_{O\alpha}-J_{\alpha\beta}}\right\} \end{aligned} \tag{4a}$$

for $t_{\max} \le 1/J_{O\alpha}$,

$$\begin{aligned} I'_2 = \frac{1}{2}\left\{[-g(t_{\max}) + 2g\left(\frac{1}{2J_{O\alpha}}\right) - g(0)]|_{J=J_{O\alpha}+J_{\alpha\beta}}\right. \\ \left. + [-g(t_{\max}) + 2g\left(\frac{1}{2J_{O\alpha}}\right) - g(0)]\Big|_{J=J_{O\alpha}-J_{\alpha\beta}}\right\} \end{aligned} \tag{4b}$$

for $1/2J_{O\alpha} \le t_{\max} \le 1/2J_{\alpha\beta}$, and

$$\begin{aligned} I'_2 = \frac{1}{2}\left\{[g(t_{\max}) - 2g\left(\frac{1}{2J_{\alpha\beta}}\right) + 2g\left(\frac{1}{2J_{O\alpha}}\right) - g(0)]\Big|_{J=J_{O\alpha}+J_{\alpha\beta}}\right. \\ \left. + [g(t_{\max}) - 2g\left(\frac{1}{2J_{\alpha\beta}}\right) + 2g\left(\frac{1}{2J_{O\alpha}}\right) - g(0)]\Big|_{J=J_{O\alpha}-J_{\alpha\beta}}\right\} \end{aligned} \tag{4c}$$

$$1/2J_{\alpha\beta} \le t_{\max} \le 3/2J_{O\alpha}.$$

Assuming $T_2 = 20$ ms, $J_{O\alpha} = 55$ Hz, and $J_{\alpha\beta} = 35$ Hz, the free induction decays and reduced integrated intensities are plotted in Figure 9. For both singly or doubly coupled C^{α}, as in Figure 9(b) and Figure 9(d) for glycine and all other amino acids, respectively, once the evolution time is above a certain value, the intensity of the decoupled experiment is higher than the non-decoupled version, even though the decoupling may cause up to ~20% ($\xi = 0.8$) signal loss. The intensity gain is most significant for evolution time of 10–15 ms, at which the intensity curves of the non-decoupled experiments plateau. For example, at 12 ms the gain is 35–69% and 19–49% for singly and doubly coupled systems, respectively, assuming $\xi = 0.8$–1.0. The threshold time strongly depends on the efficiency of the selective decoupling component, but only weakly on T_2. As shown in Figure 9(e), for most T_2 values, by acquiring 8 ms, refocusing loss of 20% can be compensated. The C^{ali}–C^{ali}–CX 3D spectrum shown in Figure 7 used $t_{2max} = 8$ ms to take this sensitivity advantage. One may also desire to acquire to 12 ms to obtain extra resolution; this digitization can be achieved within reasonable experiment time with the sequence introduced here using only 2-step phase cycle.

To simultaneously eliminate aromatic and carbonyl signals using the soft $\pi/2$ and z-filter combination demands large bandwidth (> 80 ppm). This requires eSNOB pulse as short as ~ 100 μs, which unfortunately gives inefficient excitation due to CSA recoupling (Figure 3). eBURP2 of ~ 340 μs has good excitation efficiency for on-resonance signals, but the bandwidth is still not sufficient (72 ppm). No other pulses examined meet these requirements. It is possible to use two soft $\pi/2$ pulses in series, or a cosine modulated soft $\pi/2$ pulse to cover both carbonyl and aromatic frequencies, but this will result in additional signal loss. Fortunately for the C^{ali}–C^{ali}–CX 3D as implemented in Figure 1, it is adequate to remove only C′ in t_1 because the majority of aromatic signal can be suppressed by the selective π pulse in the t_2 dimension, which selects only aliphatic signals. Here is the analysis in detail: (1) both diagonal and cross peaks of $C^{arom}(F_1)$–$C^{arom}(F_2)$ type, which are the strongest contribution, are eliminated by the soft π. (2) Spinning side bands of the C^{arom} diagonal, which are usually very weak with the MAS rates used in this study, will be aliased to the diagonal of F_1–F_2 in the aliphatic region, assuming rotor synchronized acquisition for the indirect dimensions. Therefore such signals do not interfere with aliphatic cross peaks. (3) The even weaker side bands of cross peaks among the aromatic resonances, if present, would have interfered with aliphatic cross peaks. In fact, such aromatic cross peaks can be effectively suppressed by shortening the first homonuclear mixing time (e.g. 10 ms DARR). This works since polarization transfer within an aromatic ring is optimal at longer mixing times, e.g., 50 ms (Franks et al., 2005). (4) $C^{arom}(F_1)$–$C^{ali}(F_2)$ cross peaks, mainly $C^{\gamma}(F_1)$—$C^{\beta}(F_2)$, will be preserved with $C^{arom}(F_1)$ folded into the aliphatic region. However, two facts alleviated this problem. First, there are only a small

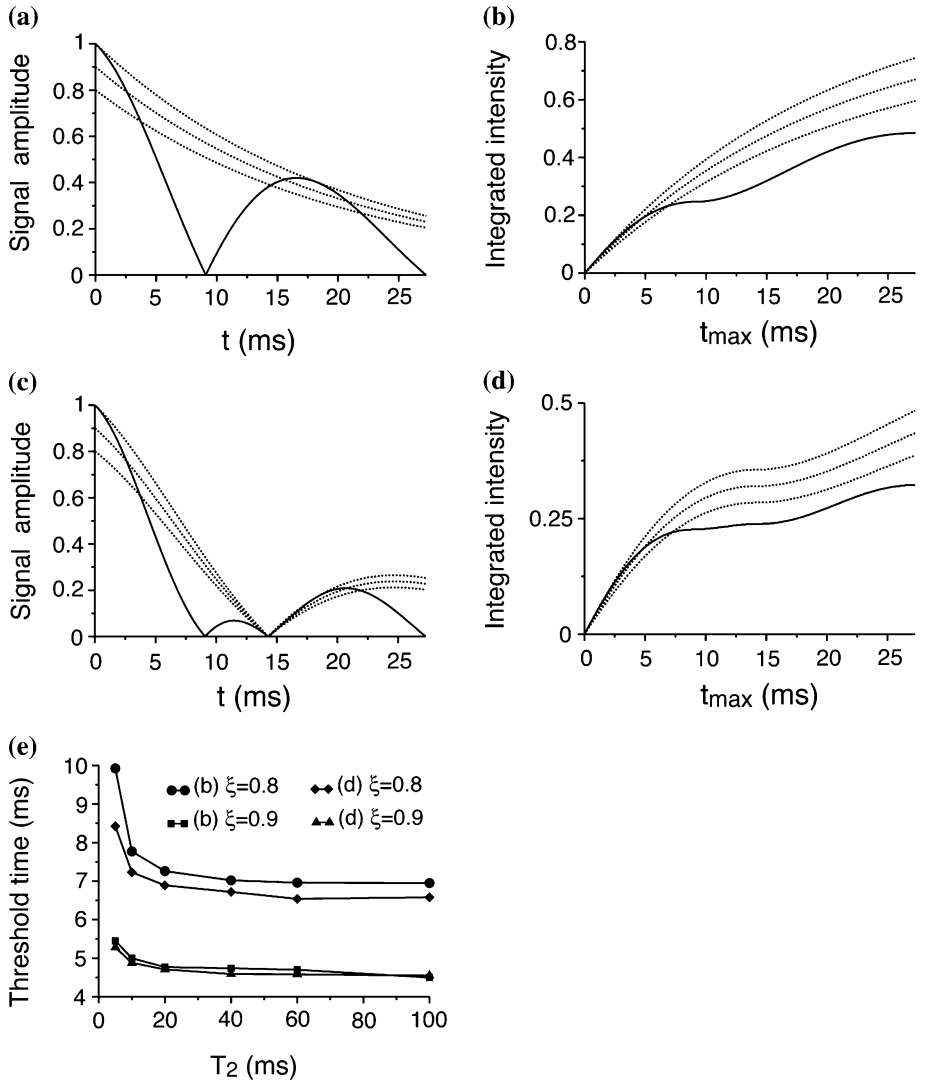

Figure 9. Intensities for non-decoupled (solid line) and$J_{O\alpha}$-decoupled (dotted lines) experiments. (a) Free induction decays (FID) for Glycine having only $J_{O\alpha}$ interaction, (b) the corresponding reduced integrated intensities defined in Eqs. (1) and (2), (c) FIDs for all other amino acids having both $J_{O\alpha}$ and $J_{\alpha\beta}$ interactions, (d) the corresponding intensities defined in Eqs. (3) and (4). (e) Dependence on T_2 relaxation time of the threshold evolution time at which the decoupled and non-decoupled experiments have identical integrated intensity. The refocusing efficiencies ξ of the soft-hard π pair were 1, 0.9, and 0.8 for the three dotted lines from top down. $J_{O\alpha} = 55$ Hz, $J_{\alpha\beta} = 35$ Hz, and $T_2 = 20$ ms were assumed.

percentage of residues in a sequence having aromatic side chain; second, they can be easily discerned by correlation to an unfolded aromatic resonance in the direct dimension.

Conclusion

We have demonstrated a novel broadband selective 3D homonulcear correlation experiment C^{ali}–C^{ali}–CX. Compared to the CX–CX–CX correlation experiment that would require a week or more under the assumptions described here, the reduced bandwidth allows a complete data set with the same digital resolution to be acquired within a half to one day. This saves experimental time by an order of magnitude in the sampling-limited cases, without sacrificing resolution offered by aliphatic carbon sites. For the sensitivity-limited cases, one may consider using C^{ali}–CX–CX, which allows a

complete data set to be acquired in 2–3 days, with the benefit of less intensity loss by using only one soft pulse. The C^{ali}–C^{ali}–CX experiment has been performed on a model protein GB1 and a fibrillar form of α-synuclein, which is implicated in Parkinson's disease. The additional dimension lifted degeneracy observed in ^{13}C–^{13}C 2D experiments. Whole spin networks of residues with various side chain lengths can be identified. Given long mixing times and/or other mixing methods, the C^{ali}–C^{ali}–CX experiment can provide sequential connectivity and structural constraints. For example, we expect that combination with glycerol labeling schemes will permit a large number of unique ^{13}C–^{13}C distances to be resolved; in this case, mixing times of ~50 ms and >200 ms would be appropriate, and the selective pulses serve the primary purpose of coherence selection and filtering (Castellani et al., 2002). The C^{ali}–C^{ali}–CX spectrum can be combined with $NC^{\alpha}CX$ and NC′CX spectra to make sequential backbone and side chain assignments.

We have found that under MAS, the soft π and π/2 pulses exhibit a complicated dependence on pulse width, especially in the short pulse limit that is necessary to select ~70 ppm region. Among the existing pulses we have tested, those having small bandwidth-duration product (such as Gaussian, SNOB, and one-lobe sinc) yield the best performance. Theoretical investigation of how MAS and CSA affects performance of these pulses may direct the design of new selective pulses that are optimal for solid samples under MAS.

Acknowledgments

This research was supported by the University of Illinois (startup funds to C.M.R), American Parkinson Disease Association (postdoctoral fellowship to D.H.Z), and the National Parkinson Foundation. The authors thank Ying Li for helpful discussion on soft pulses, John Boettcher for preparation of the GB1 sample, Dan Ladror and Kevin Hartman for preparing the A30P sample, Prof. Julia M. George (Physiology Department, University of Illinois) for the gift of A30P α-synuclein plasmid, Dr. Paul Molitor for technical assistance (VOICE NMR Facility, School of Chemistry, University of Illinois), and Heather L. Frericks for carefully reading the manuscript.

References

Abramovich, D. and Vega, S. (1993) *J. Magn. Reson. A*, **105**, 30–48.
Antzutkin, O.N., Leapman, R.D., Balbach, J.J. and Tycko, R. (2002) *Biochemistry*, **41**, 15436–15450.
Balbach, J.J., Petkova, A.T., Oyler, N.A., Antzutkin, O.N., Gordon, D.J., Meredith, S.C. and Tycko, R. (2002) *Biophys. J.*, **83**, 1205–1216.
Baldus, M., Petkova, A.T., Griffin, R.G. and Herzfeld, J. (1998) *Mol. Phys.*, **95**, 1197–1207.
Barkhuijsen, H., Beer, R.de and Ormondt, D.van (1987) *J. Magn. Reson.*, **73**, 553–557.
Bauer, C., Freeman, R., Frenkiel, T., Keeler, J. and Shaka, A.J. (1984) *J. Magn. Reson.*, **58**, 442–457.
Bax, A., Ikura, M., Kay, L.E. and Zhu, G. (1991) *J. Magn. Reson.*, **91**, 174–178.
Bennett, A.E. and Griffin, R.G. (1992) *J. Chem. Phys.*, **96**, 8624–8627.
Bennett, A.E., Rienstra, C.M., Auger, M., Lakshmi, K.V. and Griffin, R.G. (1995) *J. Chem. Phys.*, **103**, 6951–6958.
Bloembergen, N. (1949) *Physica*, **15**, 386–426.
Castellani, F., Rossum, B.V., Diehl, A., Schubert, M., Rehbein, K. and Oschkinat, H. (2002) *Nature*, **420**, 98–102.
Clayton, D.F. and George, J.M. (1998) *Trends Neurosci.*, **21**, 249–254.
Delaglio, F., Grzesiek, S., Vuister, G.W., Zhu, G., Pfeifer, J. and Bax, A. (1995) *J. Biomol. NMR*, **6**, 277–293.
Duma, L., Hediger, S., Emsley, L., Brutscher, B. and Bockmann, A. (2003a) *J. Am. Chem. Soc.*, **125**, 11816–11817.
Duma, L., Hediger, S., Lesage, A. and Emsley, L. (2003b) *J. Magn. Reson.*, **164**, 187–195.
Emsley, L. and Bodenhausen, G. (1989) *J. Magn. Reson.*, **82**, 211–221.
Emsley, L. and Bodenhausen, G. (1990) *Chem. Phys. Lett.*, **165**, 469–476.
Franks, W.T., Zhou, D.H., Wylie, B.J., Money, B.G., Graesser, D.T., Frericks, H.L., Sahota, G. and Rienstra, C.M. (2005) *J. Am. Chem. Soc.*, **127**, 12291–12305.
Geen, H. and Freeman, R. (1991) *J. Magn. Reson.*, **93**, 93–141.
Hediger, S., Meier, B.H., Kurur, N.D., Bodenhausen, G. and Ernst, R.R. (1994) *Chem. Phys. Lett.*, **223**, 283–288.
Heise, H., Hoyer, W., Becker, S., Andronesi, O.C., Riedel, D. and Baldus, M. (2005a) *PNAS*, **102**, 15871–15876.
Heise, H., Seidel, K., Etzkorn, M., Becker, S. and Baldus, M. (2005b) *J. Magn. Reson.*, **173**, 64–74.
Holdeman, T.C. and Gardner, K.H. (2001) *J. Biomol. NMR*, **21**, 383–384.
Hong, M. (1999) *J. Biomol. NMR*, **15**, 1–14.
Hutchinson, J.M.S., Sutherland, R.J. and Mallard, J.R. (1978) *J. Phys. E: Sci. Instr.*, **11**, 217–221.
Igumenova, T.I. and McDermott, A.E. (2003) *J. Magn. Reson.*, **164**, 270–285.
Jaroniec, C.P., Lansing, J.C., Tounge, B.A., Belenky, M., Herzfeld, J. and Griffin, R.G. (2001a) *J. Am. Chem. Soc.*, **123**, 12929–12930.
Jaroniec, C.P., Tounge, B.A., Herzfeld, J. and Griffin, R.G. (2001b) *J. Am. Chem. Soc.*, **123**, 3507–3519.
Kay, L.E., Marion, D. and Bax, A. (1989) *J. Magn. Reson.*, **84**, 72–84.
Kloepper, K.D., Woods, W.S., Winter, K.A., George, J.M. and Rienstra, C.M. (2006) *Protein Express. Purif.*, (in press).

Kubo, A. and McDowell, C.A. (1988) *J. Chem. Soc. Faraday Trans. I*, **84**, 3713–3730.
Kupce, E., Boyd, J. and Campbell, I.D. (1995) *J. Magn. Reson. B*, **106**, 300 .
Li, Y., Wylie, B.J. and Rienstra, C.M. (2006) *J. Magn. Reson.*, **179**, (in Press).
Marion, D., Ikura, M., Tschudin, R. and Bax, A. (1989) *J. Magn. Reson.*, **85**, 393 .
Nielsen, N.C., Bildsoe, H., Jakobsen, H.J. and Levitt, M.H. (1994) *J. Chem. Phys.*, **101**, 1805–1812.
Oas, T.G., Griffin, R.G. and Levitt, M.H. (1989) *J. Chem. Phys.*, **89**, 692–695.
Pauli, J., Baldus, M., Rossum, B.van, Groot, H.de and Oschkinat, H. (2001) *Chem. Bio. Chem.*, **2**, 272–281.
Petkova, A.T., Ishii, Y., Balbach, J.J., Antzutkin, O.N., Leapman, R.D., Delaglio, F. and Tycko, R. (2002) *PNAS*, **99**, 16742–16747.
Powers, R., Garrett, D.S., March, C.J., Frieden, E.A., Gronenborn, A.M. and Clore, G.M. (1992) *Biochemistry*, **31**, 4334–4346.
Rienstra, C.M., Hohwy, M., Hong, M. and Griffin, R.G. (2000) *J. Am. Chem. Soc.*, **122**, 10979–10990.
Straus, S.K., Bremi, T. and Ernst, R.R. (1996) *Chem. Phys. Lett.*, **262**, 709–715.
Stringer, J.A., Bronnimann, C.E., Mullen, C.G., Zhou, D.H., Stellfox, S.A., Li, Y., Williams, E.H. and Rienstra, C.M. (2005) *J. Magn. Reson.*, **173**, 40–48.
Sun, B.Q., Rienstra, C.M., Costa, P.R., Williamson, J.R. and Griffin, R.G. (1997) *J. Am. Chem. Soc.*, **119**, 8540–8546.
Suter, D. and Ernst, R.R. (1982) *Phys. Rev. B*, **25**, 6038–6041.
Suter, D. and Ernst, R.R. (1985) *Phys. Rev. B*, **32**, 5608–5627.
Szyperski, T., Yeh, D.C., Sukumaran, D.K., Moseley, H.N.B. and Montelione, G.T. (2002) *PNAS*, **99**, 8009–8014.
Takegoshi, K., Nakamura, S. and Terao, T. (2001) *Chem. Phys. Lett.*, **344**, 631–637.
Veshtort, M. and Griffin, R.G. (2004) *Chem. Phys. Chem.*, **5**, 834–850.
Wishart, D.S., Sykes, B.D. and Richards, F.M. (1991) *J. Mol. Biol.*, **222**, 311–333.
Zech, S.G., Wand, A.J. and McDermott, A.E. (2005) *J. Am. Chem. Soc.*, **127**, 8618–8626.